Application of a Front Tracking Method in Gas Metal Arc Welding (GMAW) Simulation

Guo Xu, William W. Schultz*, Elijah Kannatey-Asibu, Jr.

Department of Mechanical Engineering

University of Michigan, Ann Arbor Michigan 48109

Abstract

Background: A numerical model is developed to simulate the short-circuiting metal transfer process during gas metal arc welding (GMAW). The energy equation and the Marangoni convection are considered for the first time in analyzing the short-circuiting time.

Method of approach: A front-tracking free surface method explicitly tracks the profile of the liquid bridge. The electromagnetic field, distribution of velocity, pressure, and temperature are calculated using the developed model**.**

Results: Effects of welding current, surface tension temperature coefficient and initial drop volume on short-circuiting duration time are examined.

Conclusions: The results show that both the electromagnetic force and Marangoni shear stress play significant roles in short-circuiting transfer welding.

Keywords: Arc Welding, GMAW, Marangoni Convection

* Author to whom correspondence should be addressed. Phone: 734-936-0351; Email: schultz@umich.edu

Nomenclature

$A(\vec{U})$	Convection term in momentum equation
$\vec{B}$	Magnetic flux vector
c_p	Specific heat
f	Body force in momentum equation
$\vec{F}$	Electromagnetic force
g	Gravitational acceleration
h	Heat transfer coefficient
H	Height of computation domain
I	Welding current
j	Current density
$\vec{J}$	Current density vector
k	Thermal conductivity
L	Width of computation domain
$\vec{n}$	Normal vector of local free surface
p	Pressure
$\dot{q}$	Heat generation
r_c	Contact radius
r_w	Radius of electric wire
R	Radius of curvature
$\vec{s}$	Tangential vector of local free surface
$\vec{S}_1$	Source term in momentum equation
Δt	Time step
t	Time
T	Temperature
T_l	Liquidus temperature
T_o	Initial temperature
u	Velocity in x direction
$\vec{U}^*$	Estimated velocity vector
$\vec{U}$	Velocity vector
v	Velocity in y direction
v_{in}	Wire feed rate

V_o	Initial drop volume
x, y	Cartesian Coordinates

Greek symbols

ρ	Density
ν	Kinetic viscosity
μ	Dynamic viscosity
μ_m	Magnetic permeability
σ	Electrical conductivity
ε	Electrical resistivity
γ	Surface tension coefficient
$\vec{\tau}$	Surface stress
ϕ	Electrical potential

Subscripts

l	liquid
g	gas
x, y	components

Superscripts

n	time steps number

1. Introduction

It is well known that GMAW short-circuiting transfer is suitable for welding thin sheets due to its low average heat input. To obtain desirable weldment geometry, a thorough understanding of the bridge transfer mechanism is needed. Existing models of this process either do not consider the thermal effect or the free surface. In the early 1990s, Maruo et al [1] studied the bridging transfer of pendent mercury drops. Time dependent deformation of the liquid bridge was observed by high-speed photography. Effects of current on the neck diameter and the short-circuiting time were dynamically simulated using the Marker and Cell (MAC) method. Their study showed that metal transfer was driven jointly by electromagnetic and capillary forces.

Hirata et al [2] developed a one-dimensional model of the GMAW short-circuiting transfer. They found that, in addition to the short-circuiting current level, the initial drop volume also played a role in determining the breakup time. Using the Volume of Fluid (VOF) method, Choi et al [3] analyzed the effects of welding current, initial drop volume, and wire feed rate on short-circuiting transfer. They determined that the welding current is the sole dominating factor in the dynamics of short-circuiting transfer. However, by considering only the isothermal case, this study is incapable of accounting for the Marangoni shear stress. Choi et al [4] subsequently included drop development into a simplified short-circuiting model. Drop growth was simulated by the characteristic equation of an electric wire. The force balance model was adopted to determine the drop detachment. Welding current, voltage and metal transfer mode were only

qualitatively predicted due to over-simplification. Wang [5] developed a numerical model for plug welding of a multi-layered workpiece. The short-circuiting welding process he proposed has the advantage of reducing welding spatter and lowering porosity.

Thus far, the effect of temperature distribution in GMAW short-circuiting metal transfer has not been addressed.

The paper is organized as follows. Section 2 describes the benchmarking of the front tracking method used to represent the free surface in GMAW short-circuiting transfer. Following the mathematical formation for the short-circuiting transfer in section 3, section 4 discusses the solution procedure and numerical consideration of the given governing equations. Section 5 presents the effects of welding current, surface tension temperature coefficient and initial drop volume on short-circuiting duration time. The conclusions are given in section 6.

2. Free surface method

The GMAW short-circuiting bridge has a free surface. Study of free-surface problems has been limited due to the difficulties associated with interface representation, and computation of surface tension effects. One of the most traditional approaches to computing multiphase flows, the MAC method developed by Harlow and Welch [6], places massless tracer particles in the fluid field that move with the fluid velocity. This method is sometimes considered inefficient

since computer storage can become prohibitively large while each particle is traced individually. In recent years, the VOF [7] method has gained popularity in simulating moving boundary problems. It introduces a fraction function, *F*, to represent the volumetric percentage of fluid in each cell. Tracking of the interface is achieved by advecting the fluid flux in each cell after the velocities are computed on a fixed grid. Due to its intuitive denotation of the fluid field, the VOF method has also seen application in the simulation of GMAW metal transfer. However, the shape of interfaces reconstructed from the VOF method is inherently poor with complicated smoothing algorithms being required to reconstruct the surface. As a result, surface tension computation is often inaccurate.

Ashgriz and Poo [8] presented a technique, FLAIR (Flux Line-segment Model for Advection and Interface Reconstruction), which represents the fluid interface by sloped line segments at the boundary of neighboring cells. Relocation of interface is achieved by moving the discrete line segments with local velocity at the cell boundaries. Brackbill [9] developed a continuum surface force model (CSF) in which the interface between different fluids is artificially expanded into a transitional region of finite thickness. Discontinuities of fluid properties including surface tension are approximated by a continuous function within the transition region. This approach allows for a ‘one-field’ description of the multiphase system and consequently eliminates the need for applying interfacial boundary conditions because they are absorbed by the governing equations.

In this paper, a newer boundary capturing technique, proposed by Unverdi and Tryggvason [10], is implemented to handle the free surface (profile of liquid bridge). Formulated on a fixed grid where the governing equations are solved, this method uses a moving grid of lower order (the so-called “front”) to explicitly track the free surfaces. This technique not only makes surface tension computation effortless, but also delivers high quality boundaries. Figure 1 is a schematic representation of this method.

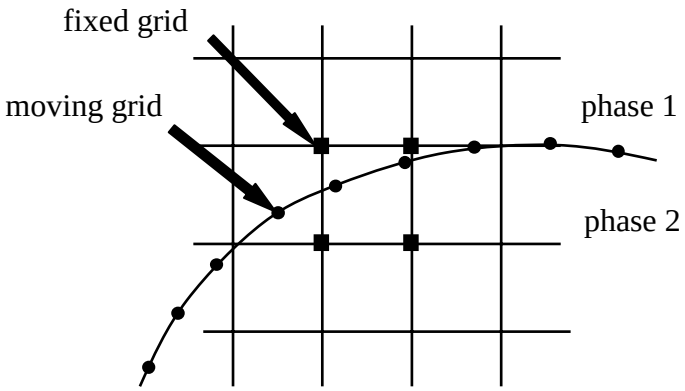

Fig. 1 Schematic representation of front tracking method

Benchmarking of the Front Tracking Method

To test the performance of the above-described algorithm, it was used to simulate an initially static drop situated in another medium, as shown in Fig. 2. With surface tension being the only driving effect, the drop will start to oscillate. A ‘front’ was put at the interface. Parameters used for simulation are shown in Table 1. The problem is nondimensionalized by picking the width of the computational domain *W*, the liquid density ρ_{in} and viscosity μ_{in} as the basic scales.

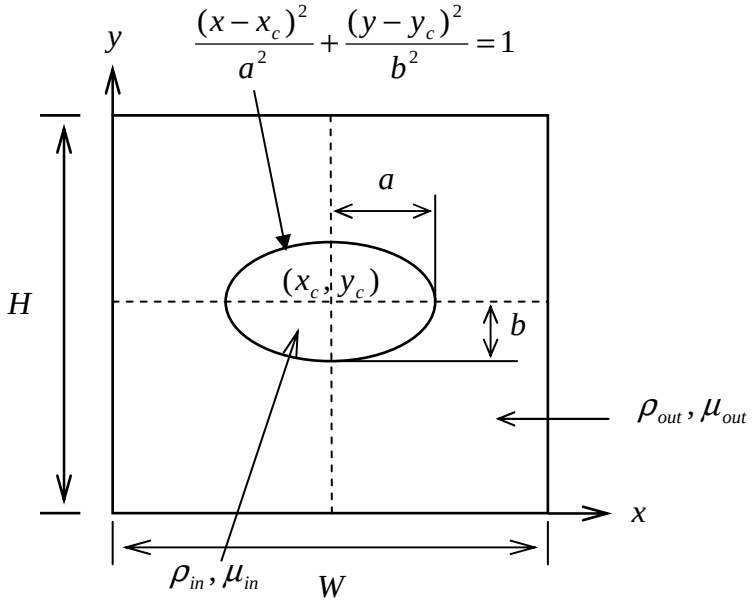

Fig. 2 Problem set-up

Table 1. Parameters used in isothermal simulation

	Dimensional	Nondimensional
Computation domain	W = 0.005m, H = 0.005m	W = 1.0, H = 1.0
Bubble dimension	a = 0.001m, b = 0.0005m	a = 0.2, b = 0.1
Outer density, ρ_{out}	400 kg/m^3	0.4
Inner density, ρ_{in}	1000 kg/m^3	1.0
Outer viscosity, μ_{out}	0.01 kg/m.s	1.0
Inner viscosity, μ_{in}	0.001 kg/m.s	0.1
Surface tension coefficient	0.01N/s	50000
Gravity	0 m/s^2	0

A series of numerical experiments examine the effects of density ratio, viscosity ratio, time step, and grid resolution on computation. Table 2 summarizes the design of numerical experiments. The vertical position of the top of the drop Y_m is plotted with time in Figs. 3-7.

Table 2. Design of numerical experiment

	Computation Time (min)	Density ratio (ρ_{in}/ρ_{out})	Viscosity ratio (μ_{in}/μ_{out})	Grid	Time step
Density	40	2.5	10	60 * 60	dynamic
1 cycle	21	5	10	60 * 60	dynamic
	10	10	10	60 * 60	dynamic
	14	25	10	60 * 60	dynamic
	20	50	10	60 * 60	dynamic
	37	100	10	60 * 60	dynamic
	56	150	10	60 * 60	dynamic
viscosity	16	10	2.5	60 * 60	dynamic
1 cycle	11	10	5	60 * 60	dynamic
	10	10	10	60 * 60	dynamic
	33	10	25	60 * 60	dynamic
	75	10	50	60 * 60	dynamic
	90	10	100	60 * 60	dynamic
time step	70	10	10	60 * 60	1E-6
1 cycle	63	10	10	60 * 60	2E-6
	31	10	10	60 * 60	4E-6
	25	10	10	60 * 60	8E-6
	14	10	10	60 * 60	1.60E-5
space	2	10	10	15 * 15	4E-6
1 cycle	8	10	10	30 * 30	4E-6
	18	10	10	45 * 45	4E-6
	31	10	10	60 * 60	4E-6
	48	10	10	75 * 75	4E-6
	71	10	10	90 * 90	4E-6
	103	10	10	105 * 105	4E-6
	85	10	10	120 * 120	4E-6
	228	10	10	150 * 150	4E-6
3 cycles	14	2.5	10	30 * 30	dynamic
	55	2.5	10	60 * 60	dynamic
	354	2.5	10	110*110	dynamic
	4	25	10	30 * 30	dynamic
	21	25	10	60 * 60	dynamic

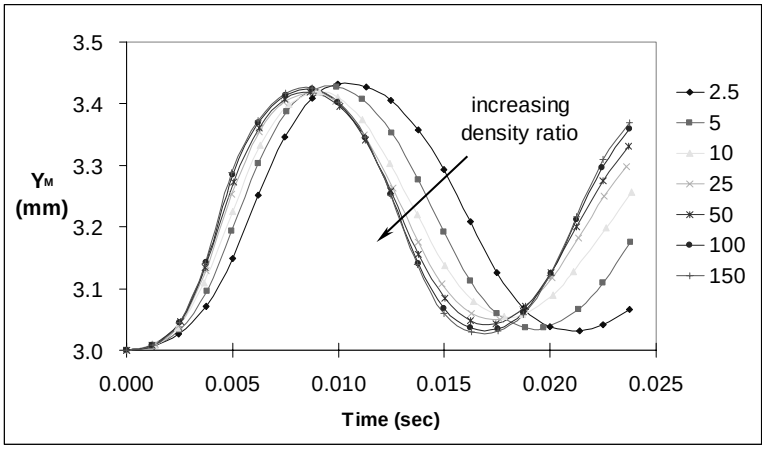

Figure 3. Effect of density ratio on isothermal drop oscillation (60×60 grid)
(Y_M: vertical coordinate of the top of the drop)

Table 3. Oscillation period versus density ratio

Density ratio	2.5	5	10	25	50	100	150
Period (sec)	0.0214	0.0193	0.0183	0.0174	0.0171	0.0169	0.0168

Fig. 3 and Table 3 show that increasing density ratio decreases the period. Higher ratios increase convergence problems, in that negative densities may appear when smoothing the density field near interfaces. However, it can be projected that a density ratio of $\rho_{in} / \rho_{out} = \infty$ may be reasonably approximated by Richardson extrapolation to give a period of 0.01671 second. Also, as shown in Table 2, it is found that the front tracking code used results in the least computational effort when ρ_{in} / ρ_{out} is around 10.

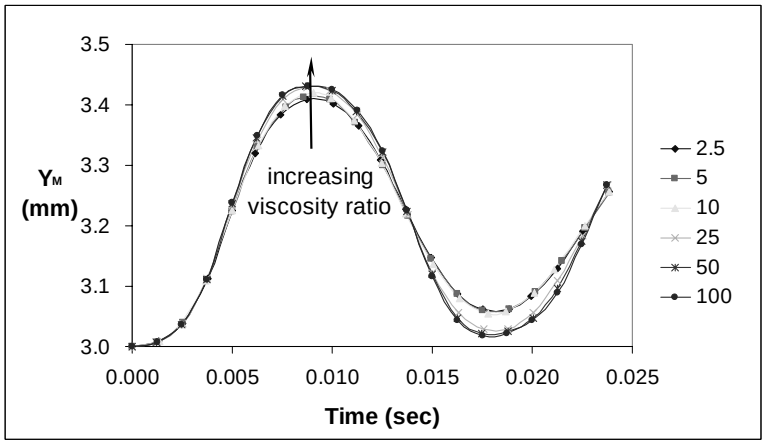

Figure 4. Effect of viscosity ratio on isothermal drop oscillation (60×60 grid)

Table 4. Oscillation period versus viscosity ratio

Viscosity ratio	2.5	5	10	25	50	100
Period (sec)	0.0178	0.0177	0.0176	0.0175	0.0175	0.0175

The effect of viscosity ratio is shown in Fig. 4 and Table 4. Similar to Fig. 3, μ_{in} / μ_{out} =100 appears to present a reasonable approximation of $\mu_{in} / \mu_{out} = \infty$.

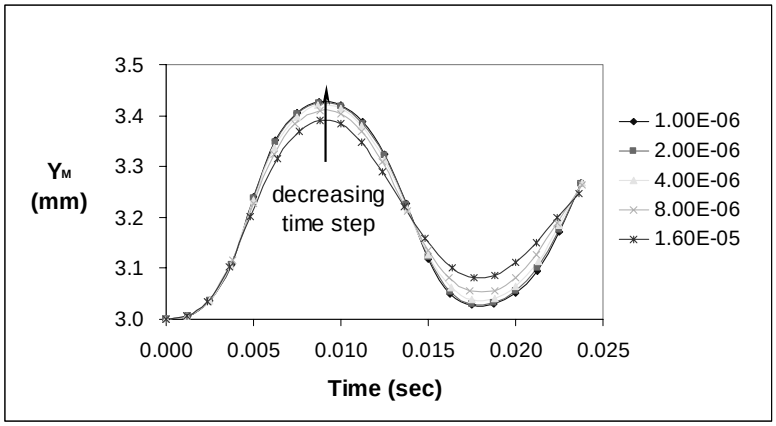

Figure 5. Effect of time step

Table 5. Oscillation period versus time step

Time step (sec)	$1x10^{-6}$	$2x10^{-6}$	$4x10^{-6}$	$8x10^{-6}$	$16x10^{-6}$
Period (sec)	0.0179	0.0180	0.0180	0.0182	0.0182

Fig. 5 and Table 5 show the effect of computational time step. It can be seen that $\Delta t = 4x10^{-6}$ sec provides almost identical results with $\Delta t = 2x10^{-6}$ sec and $\Delta t = 1x10^{-6}$ sec.

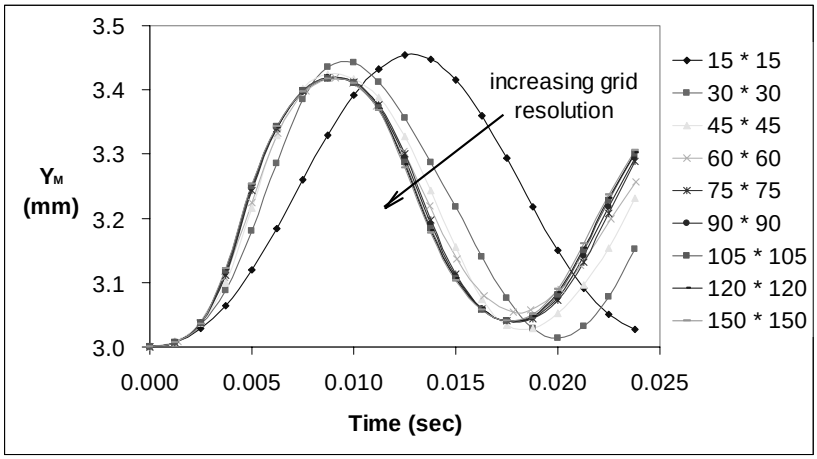

Figure 6. Effect of mesh resolution

Table 6. Oscillation period versus mesh resolution

Grid	15×15	30×30	45×45	60×60	75×75	90×90	105×105	120×120	150×150
Period (sec)	0.0242	0.0200	0.0182	0.0178	0.0176	0.0175	0.0175	0.0175	0.0175

Fig. 6 and Table 6 show the effect of mesh resolution. As can be seen, a resolution of 60×60 provides satisfactory accuracy.

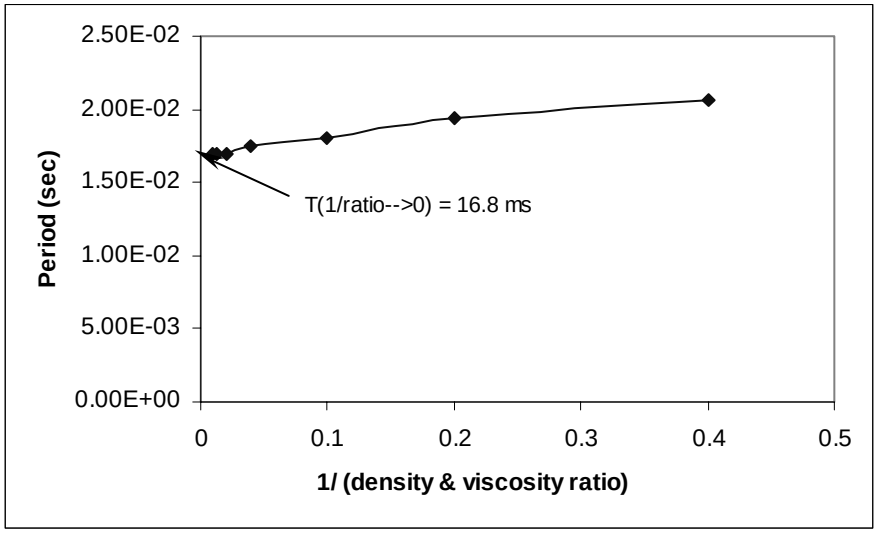

Fig. 7 Oscillation period versus density and viscosity ratios

As shown in Fig. 7, the oscillation period of the drop was plotted versus the density and viscosity ratios (set to be the same). It was found that with increasing density and viscosity ratios the period decreases. Note that though our code has difficulty handling practically infinite density and viscosity ratios, this oscillation period, 0.0168 sec, was accurately predicted by a density ratio of 150 and viscosity ratio of 100.

The same problem was also simulated using the VOF method. Since VOF can only simulate a single phase, the effect of media around the drop was not considered. This is equivalent to an infinite density and viscosity ratios in the front tracking method. Though an infinite density or viscosity ratio cannot be practically implemented in the front tracking method, we know from the discussion above that a modest ρ_{in} / ρ_{out} and μ_{in} / μ_{out} may provide sufficient accuracy. Fig. 8

compares the computation results from both front tracking and VOF, showing the shape of the drop at different times. Parameters used for the comparison are listed in Table 7.

Table 7. Parameters used for comparison

ρ_{in}/ρ_{out}	μ_{in}/μ_{out}	Grid	Time step
25	25	60*60	4E-6

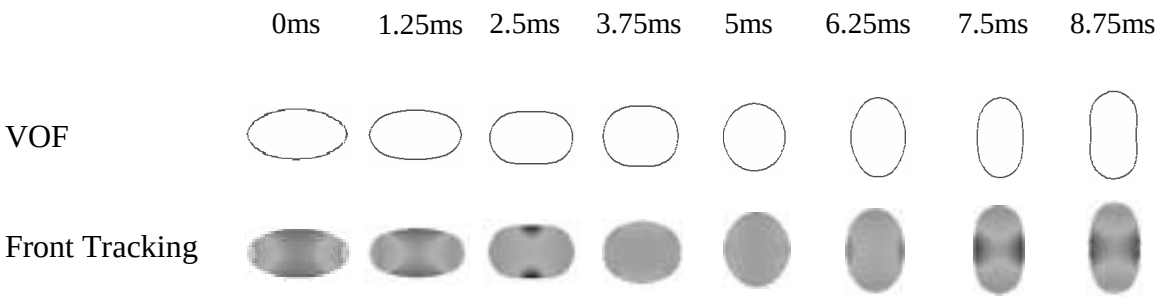

Fig. 8. Comparison between the front tracking and VOF methods

3. Formulation

Governing Equations

Material properties of all fluids are taken as constant. Buoyancy force is neglected due to its generally small magnitude compared to the electromagnetic force [11]. The governing equations described below are valid for the entire fluid field (liquid metal and gas). The flow field during the welding process will be three-dimensional, unless spot welding is considered and

axisymmetry can be assumed. Here, we study the qualitative effects in a two-dimensional simulation, without relative lateral motion between the workpiece and the electrode.

The governing equations are:

Continuity:

$$\frac{\partial u}{\partial x}+\frac{\partial v}{\partial y}=0 \tag{1}$$

Momentum:

$$\rho\frac{\partial u}{\partial t}+\rho\left(u\frac{\partial u}{\partial x}+v\frac{\partial u}{\partial y}\right)=-\frac{\partial p}{\partial x}+\mu\left(\frac{\partial^2 u}{\partial x^2}+\frac{\partial^2 u}{\partial y^2}\right)+f_x \tag{2}$$

$$\rho\frac{\partial v}{\partial t}+\rho\left(u\frac{\partial v}{\partial x}+v\frac{\partial v}{\partial y}\right)=-\frac{\partial p}{\partial y}+\mu\left(\frac{\partial^2 v}{\partial x^2}+\frac{\partial^2 v}{\partial y^2}\right)+f_y \tag{3}$$

Energy:

$$\rho c_p\left(\frac{\partial T}{\partial t}+u\frac{\partial T}{\partial x}+v\frac{\partial T}{\partial y}\right)=k\left(\frac{\partial^2 T}{\partial x^2}+\frac{\partial^2 T}{\partial y^2}\right)+\dot{q} \tag{4}$$

where the components of body force, f_x and f_y, are usually dominated by the electromagnetic force. However, in the front tracking method, surface tension and Marangoni shear stress are also treated as 'body forces' concentrated at the free surface. In two-dimension, the stresses due to surface tension are given by

$$\vec{\tau}=\frac{\gamma}{R}\vec{n}+\frac{\partial\gamma}{\partial T}\cdot\frac{\partial T}{\partial s}\vec{s} \tag{5}$$

where γ is the surface tension coefficient, R is the radius of curvature $\partial\gamma/\partial T$ is the surface tension temperature coefficient, $\vec{s}$ and $\vec{n}$ are tangential and normal to the interface, respectively. The plasma shear stress is neglected because according to Choo and Szekely [12], it is insignificant in low and modest current regimes when compared to the Marangoni shear stress. In the energy equation, $\dot{q}$ is the heat generation due to Joule heating.

Electromagnetic Force

Based on the steady state Maxwell's equations with the magnetohydrodynamics (MHD) approximation [13], the electromagnetic force can be calculated by the following equations [14]:

Poisson equation for the electrical potential

$$\Delta\phi = 0 \tag{6}$$

Ohm's law

$$\vec{J} = -\sigma\nabla\phi \tag{7}$$

Ampere's law

$$\nabla \times \vec{B} = \mu_m \vec{J} \tag{8}$$

Electromagnetic force

$$\vec{F} = \vec{J} \times \vec{B} \tag{9}$$

where ϕ is the electrical potential, $\vec{J}$ is the current density vector, σ is the electrical conductivity, $\vec{B}$ is the magnetic flux vector, μ_m is the magnetic permeability, and $\vec{F}$ is the electromagnetic force.

Boundary Conditions

Fig. 9 gives the boundary conditions for velocity, pressure, temperature, and electrical potential. Initially the molten drop and the weld pool are in contact, and the weld pool surface is assumed flat. The computation region only includes molten metal and gas, not the melting or solidified metal. In Fig. 1(a), the normal velocity along the top boundary is set equal to the wire feed rate, while free-slip conditions are applied for velocities at the other three boundaries. Mixed temperature boundary conditions are applied as shown in Fig. (1b). In Fig. 1(c), both inflow and outflow current densities are assumed to be uniform.

Free surface boundary conditions on current and temperature are obviated by again having the electrical and thermal properties vary continuously across the gas-solid interface. Here we have tested and used density, viscosity, electrical conductivity, and specific heat ratios of 50:1. The results show relative insensitivity to the ratio used. Because we have no arc model, the simulations are not very meaningful after necking is complete.

$$j_{in} = \frac{I}{\pi r_c^2} \tag{10}$$

$$j_{out} = \frac{I}{\pi L^2 + 2\pi L H_1} \tag{11}$$

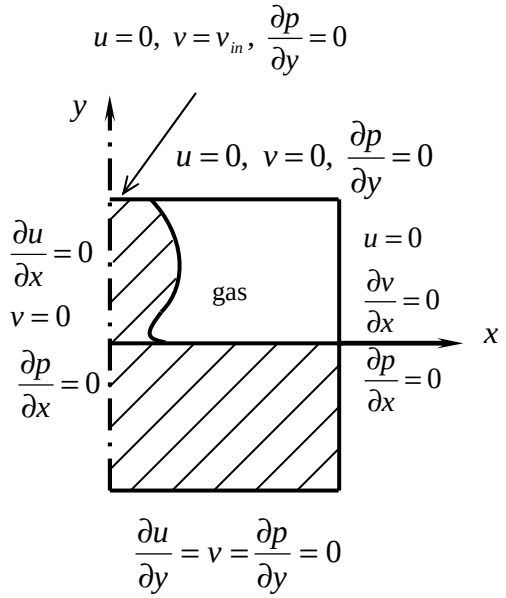

(a) Velocity and pressure

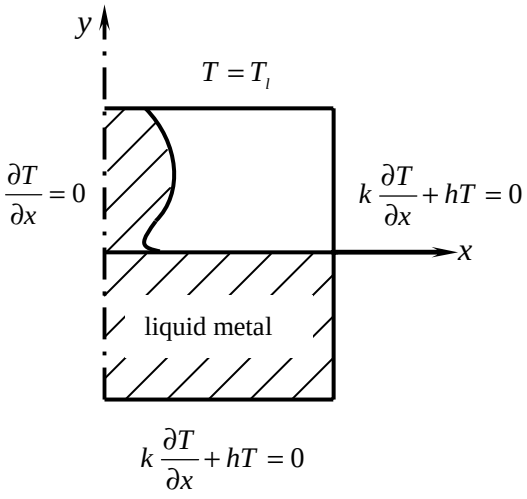

(b) Temperature

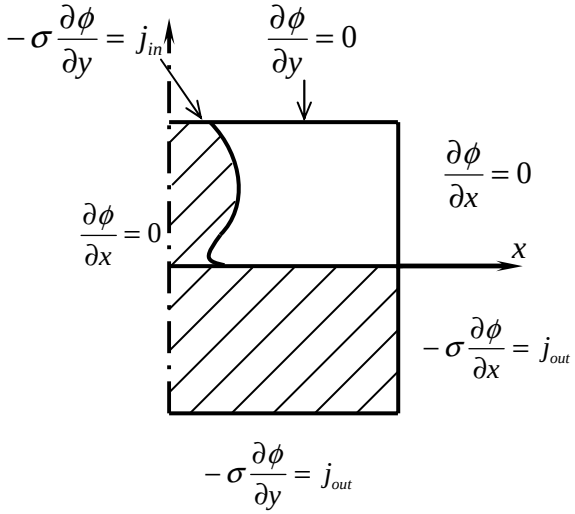

(c) Electrical Potential

Fig. 9 Boundary conditions

Initial Conditions

Fig. 10 summarizes the initial conditions for initial drop geometry. The initial drop volume is defined as the amount of fluid between the electrode and the undisturbed weld pool surface ($0 < y < 2h$), and can be calculated by

$$V = \pi R_o (R_o^2 + a^2)\sin\theta - \frac{1}{3}\pi R_o^3 \sin^3\theta - \frac{1}{2}\pi R_o^2 a(2\theta + \sin 2\theta) \tag{12}$$

where $R_o = \sqrt{(a + r_c)^2 + h^2}$, $\theta = \sin^{-1}(h/R_o)$.

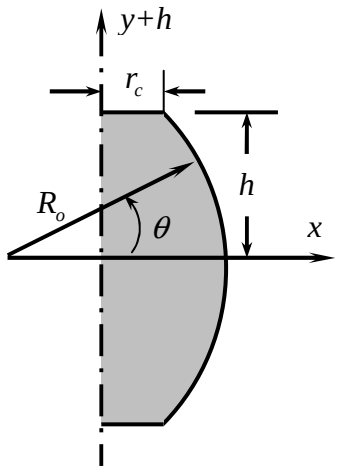

Fig. 10 Initial geometry. Additionally, $u(t=0)=0, v(t=0)=0$ and $T(t=0)=T_l$)

4. Numerical Considerations

The governing equations, including Maxwell's equations, are solved on a fixed staggered grid where scalar and vector quantities are placed at the center and sides of mesh cells, respectively. The solution procedure is as follows:

(1) Calculate the electromagnetic force from eq. (6-9).

(2) Calculate the surface tension and the Marangoni shear stress on the 'front' from eq. (5). Then convert the quantity to the fixed grid. This transformation takes the form

$$\phi_{ij} = \sum_{l} \phi_l w_{ij} \frac{\Delta l}{h^2} \tag{13}$$

where ϕ_l and ϕ_{ij} are front and fixed grid values, Δl is the length of front elements, h is the size of mesh cells, w_{ij} are weights, which in two dimensional cases satisfy

$$\sum_{ij} w_{ij} = 1 \tag{14}$$

and usually take the form of

$$w_{ij}(x_p) = d(x_p - ih)d(x_p - jh) \tag{15}$$

We use a weighting function suggested by Peskin [15]:

$$d(r) = \begin{cases} \frac{1}{4h}\left(1 + \cos\frac{\pi r}{2h}\right), & |r| < 2h \\ 0, & |r| \geq 2h \end{cases} \tag{16}$$

(3) In the mathematical model, velocity and pressure are coupled by the continuity and momentum eq. (1-3). In this paper a projection method, described below, is used to decompose the $\vec{U} \sim p$ relationship.

(i) Predict velocity at the new time step

$$\vec{U}^{*} = \vec{U}^{n} + \Delta t\left[-A(\vec{U}^{n}) + \nu\nabla^2\vec{U}^{n} + \vec{S}_1\right] \tag{17}$$

(ii) Solve the Poisson equation for pressure

$$\nabla^2 p = \frac{\rho}{\Delta t}\nabla \cdot \vec{U}^* \tag{18}$$

(iii) Correct the estimated velocity

$$\vec{U}^{n+1} = \vec{U}^* - \frac{\Delta t}{\rho}\nabla p \tag{19}$$

(iv) Solve the energy equation, where the heat generation term is calculated by

$$\dot{q} = \varepsilon\left(j_x^2 + j_y^2\right) \tag{20}$$

where ε is the electrical resistivity and j_x and j_y are components of current density.

(v) Advance fronts by interpolating the Euler velocity solved from step (3). The fixed grid velocity is transformed to the 'front' velocity by eq. (13).

(vi) March to the next time step and go back to step (i). Repeat this process until the liquid bridge breaks up. When the minimum diameter of the liquid bridge decreases below the size of one cell dimension, breakup is said to happen and the computation stops.

The size of the computation domain is $4mm \times 6mm$, discretized into a uniform grid of 24×36 nodes. The time step is dynamically adjusted to ensure computational stability. The initial temperature is assumed to be uniform.

5. Results and discussion

The liquid metal is assumed to be 304 stainless steel surrounded by Argon gas. Table 8 summarizes the physical properties used in the simulation [16,17]. Room temperature physical properties of Argon are used. The 1.2mm diameter wire feed rate is prescribed as $70\text{mm}/\text{s}$. For a Fe-S system, $\partial\gamma/\partial T$ is a function of temperature and sulfur concentration. For temperatures between 1700K and 3000K, and a 200 ppm sulfur concentration, $\partial\gamma/\partial T$ varies from -4×10^{-4} to $6\times10^{-4}\,\text{N}/\text{m}\cdot\text{K}$ [18]. In this paper, $\partial\gamma/\partial T$ is taken as a constant, and both positive and negative coefficients are used to investigate the effect of the Marangoni shear stress. Under the same temperature range and sulfur concentration, the variation of surface tension is small (from 1.5 N/m to 1.64 N/m). Therefore γ is also approximated as a constant in this paper in the normal stress boundary condition.

Table 8. Material properties used for simulation

Symbol	Value (unit)
c_{pg}	$0.53\ \mathrm{J/kg\cdot K}$
c_{pl}	$780\ \mathrm{J/kg\cdot K}$
g	$9.8\ \mathrm{m/s^2}$
h	$80\ \mathrm{W/m^2\cdot K}$
H	$6\ \mathrm{mm}$
k_g	$1.8\ \mathrm{W/m\cdot K}$
k_l	$22\ \mathrm{W/m^2\cdot K}$
L	$4\ \mathrm{mm}$
r_c	$0.6\ \mathrm{mm}$
r_w	$0.6\ \mathrm{mm}$
T_l	$1727\ \mathrm{K}$
T_o	$1727\ \mathrm{K}$
ρ_g	$16.3\ \mathrm{kg/m^3}$
ρ_l	$6900\ \mathrm{kg/m^3}$
μ_g	$1.81\times10^{-5}\ \mathrm{kg/m\cdot s}$
μ_l	$0.006\ \mathrm{kg/m\cdot s}$
σ_g	$6.3\times10^{2}\ \Omega^{-1}\mathrm{m}^{-1}$
σ_l	$7.4\times10^{5}\ \Omega^{-1}\mathrm{m}^{-1}$
μ_{mg}	$4\pi\times10^{-7}\ \mathrm{H/m}$
μ_{ml}	$4\pi\times10^{-7}\ \mathrm{H/m}$
ε	$4.32\times10^{-6}\ \Omega\cdot\mathrm{m}$
γ	$1.5\ \mathrm{N/m}$

Free Surface Profile

Fig. 11 shows the transient bridge free surface profile for a variety of welding currents. For currents of 100A, 150A and 200A, the short-circuiting time is found to be 11.02ms, 8.82ms and

7.66ms respectively. For 100A current, necking first occurs in the middle of the liquid bridge and eventually breaks up there. With increased current the breakup happens sooner and the point of breakup moves downward toward the weld pool. This trend is consistent with Choi [3].

(a) Welding current I = 100A

(b) Welding current I = 150A

(c) Welding current I = 200A

Fig. 11 Bridge profiles for various welding currents

Neck Diameter

Fig. 12 shows the transient evolution of neck diameter (smallest diameter of the liquid bridge) and maximum current density through the bridge. For 100A current, the liquid bridge profile is quite stable before 4.7ms, implying that the effect of the electromagnetic force is insignificant in the early stages. Necking starts around 4.7 ms, and the time evolution of both the neck diameter and maximum current density is nearly linear until breakup happens. The high frequency

variation in the current density curve is mainly due to numerical error. For the 150A current, the necking curve starts deflecting around 4.3ms. Further increasing current to 200A results in an almost linearly developing current density, and the diameter curve deflects at around 4.0ms.

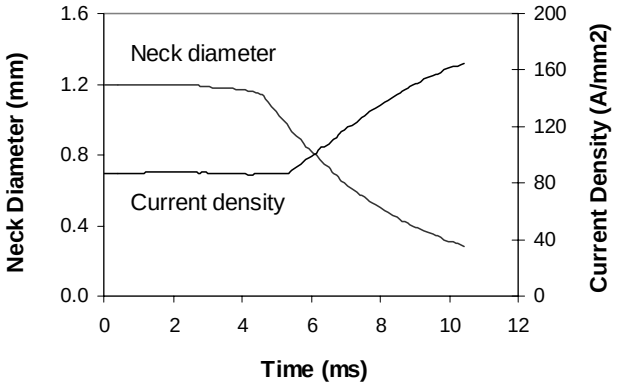

(a) Welding current I = 100A

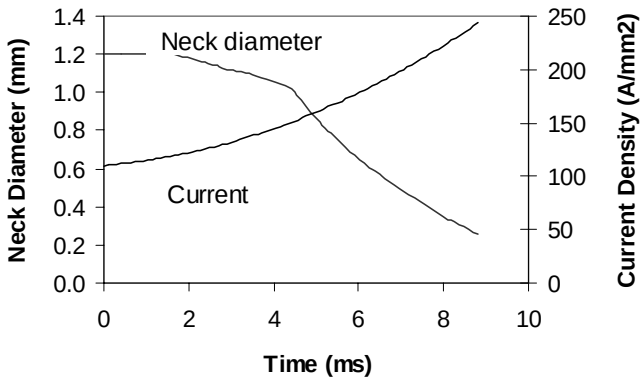

(b) Welding current I = 150A

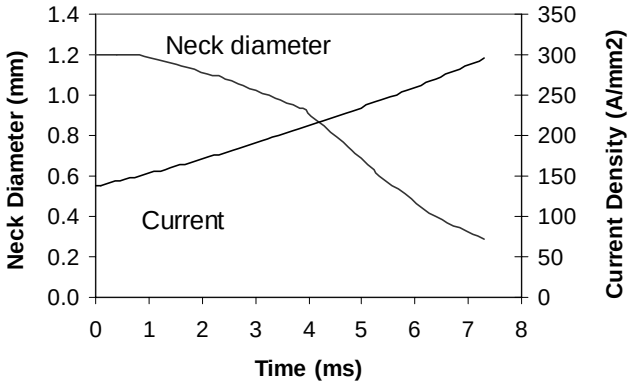

(c) Welding current I = 200A

Fig. 12 Neck diameter and maximum current density

Velocity Distribution

Fig. 13 shows the velocity distribution at 5.5ms for currents of 100A and 150A. The velocity profile is characterized by a strong flow in the axial direction. The jet velocity profile persists well into the weld pool loop, driven by the electromagnetic force. This trend was also shown by Choi et al [3]. The maximum velocities are found to be 1.3 m/s and 1.8m/s for 100A and 150A respectively.

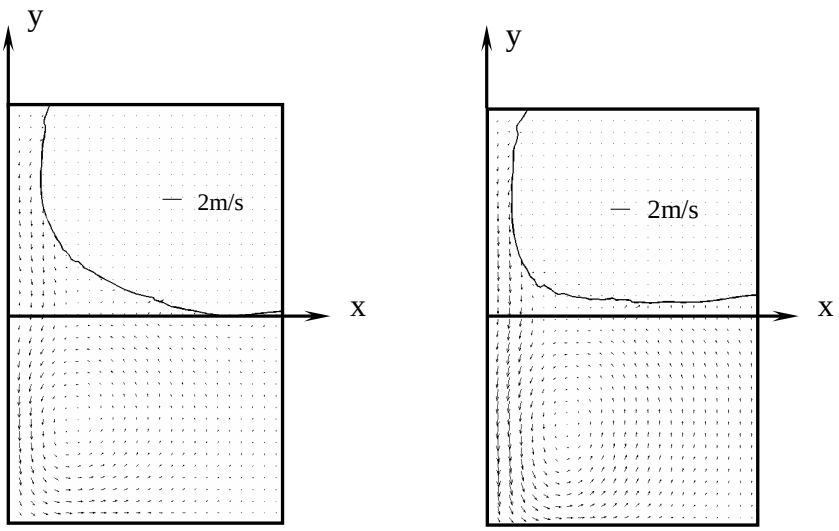

(a) I = 100A, t = 5.5ms (b) I = 150A, t = 5.5ms

Fig. 13 Velocity distribution for two currents. The arrow shows the scale for the velocity vectors. The left boundary is a line of symmetry and the right is the computational boundary.

Initial Drop Volume

We found that the initial drop volume made an insignificant contribution on short-circuiting time. For example, incrementing the initial drop volume by 50% percent, from 6.3 mm^3 to 9.5 mm^3, increases the short-circuiting time by less than 4%, from 10.6ms to 11ms. It appears that the initial configuration is not important and the solution could be determined by having a 'cylindrical' drop, and letting R_c = constant all the way to the weld pool at $t = 0$.

Marangoni Effect

To include the Marangoni effect in GMAW short-circuiting transfer simulation, we must solve the temperature distribution. Fig. 14 shows a snapshot in time for the same simulation presented in Fig. 15. Note that in both cases the maximum temperature appears at the bridge neck. During necking, the welding current has to pass through a decreased cross-sectioned area, resulting in a significant increase in the current density. Consequently, the Joule heating rapidly increases the local temperature.

To show the Marangoni effect, we use three constant values of the surface tension temperature coefficient: -0.0002, 0, and 0.0002 $N/m \cdot K$. Fig. 15 shows that the short-circuiting time increases as the surface tension temperature coefficient changes from negative to positive. For a negative coefficient, the bridge reaches the breakup stage after 8.82ms, while for zero and positive coefficients, it takes 8.94ms and 9.17ms, respectively, to break up the bridge. This can

be explained by considering the temperature distribution in Fig. 14. For a negative coefficient, since the maximum temperature occurs at the neck area where surface tension is the smallest, the Marangoni shear stress pulls liquid away from that area, aiding the break up of the bridge by the electromagnetic force. Following the same logic, for positive coefficient, the Marangoni shear stress and electromagnetic force counteract each other, slowing down the breakup process. Thus in addition to the electromagnetic force, the Marangoni shear stress is also a key factor in controlling GMAW metal transfer rate and breakup.

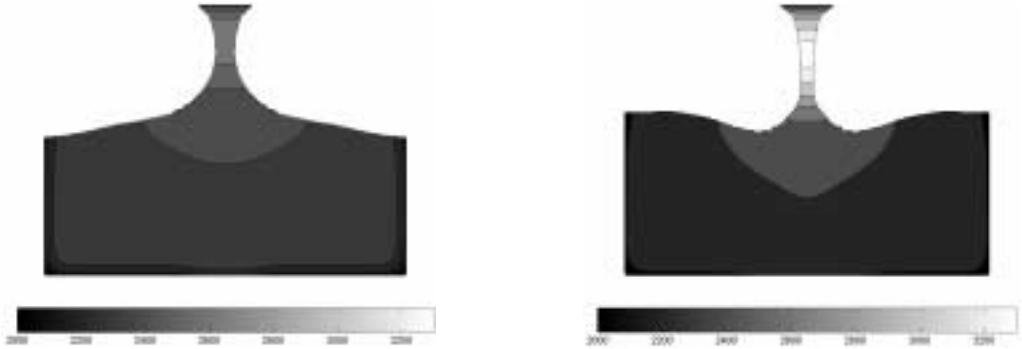

(a) t = 8.5ms, I = 100A (b) t = 8.5ms, I = 150A

Fig. 14 Temperature distribution ($\partial\gamma/\partial T = -0.0002$ N / m · K)

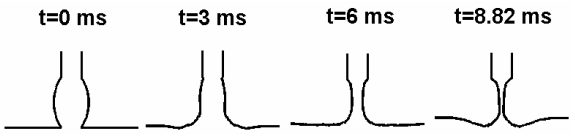

(a) Negative coefficient ($\partial\gamma/\partial T = -0.0002\ \ N/m\cdot K$)

(b) Zero coefficient (Isothermal)

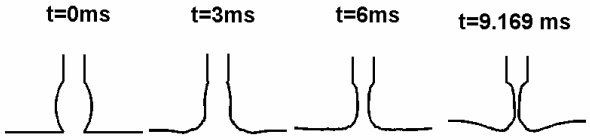

(c) Positive coefficient $\left(\partial\gamma/\partial T = 0.0002\ \ N/m\cdot K\right)$

Fig. 15 Marangoni Effect (I = 150A)

6. Conclusion

As shown by the bridge profile for various welding currents, higher welding currents result in faster breakup because of the greater electromagnetic pinch effect. The neck diameter and the current density at the neck under high current (200A) varies almost linearly with time, while their change is not obvious in the early stages of short-circuiting transfer under lower currents (100A and 150A). The velocity distribution for 100A and 150A both demonstrate a strong fluid flow away from the electrode at and near the symmetry axis within the weld pool. This pattern causes the pool surface away from the short-circuiting region to be elevated and the short-circuiting region near the axis is depressed.

Many factors affect short-circuiting transfer. The initial conditions as represented by the initial drop volume between the electrode and pool are relatively insignificant in affecting the breakup times. However, the Marangoni effect does play an important role in determining the short-circuiting duration time. The short-circuiting time increases as the surface tension temperature coefficient changes from negative to positive.

The front tracking method used in this paper provides a convenient representation of the free surfaces in GMA short-circuiting transfer. There are several property ratios involved in the front tracking method simulation described in this paper, namely, density ratio, viscosity ratio, heat conductivity ratio, specific heat ratio, magnetic permeability ratio, and electrical conductivity ratio. These ratios range from around one to several thousand. High ratios cause convergence problems as discussed in section 2, “Free surface method”. However, as shown by the benchmarking of this front tracking method, an infinite ratio may be reasonably approximated by a modest value (we used density ratio ρ_l/ρ_g , viscosity ratio μ_l/μ_g , electrical conductivity ratio σ_l/σ_g , and specific heat ratio c_{pl}/c_{pg} of 50:1) without introducing significant errors.

In this study, the wire melting rate is set to be equal to the wire feed speed so that the liquid solid interface is not moving in the absolute coordinate system. Future study, however, should allow a moving molten line and rupture of the drops for a more complete understanding of the short-circuiting process. In addition, more consideration is needed in the third direction with a translating electrode to extend the analysis from the spot welding mode discussed here.

References

[1] Maruo, H., Hirata, Y., and Goto, N., 1992, “Bridging Transfer Phenomena of Conductive Pendent Drop,” Quart. J. Japan Welding Society, **10**, pp. 43-50.

[2] Hirata, Y., Osamura, T., Goto, N., and Ohji, T., 1993, “Numerical Model of Short-Circuiting Transfer Process in GMA Welding,” *Seventh International Conference on Computer technology in Welding*, NIST, Washington D.C., pp. 279-287.

[3] Choi, S. K., Ko, S. H., Yoo, C. D., and Kim, Y. S., 1998, “Dynamics Simulation of Metal Transfer in GMAW - Part 2: Short-Circuiting Transfer Mode,” Welding J., **77**, pp. 45s-51s.

[4] Choi, J. H., Lee, J. Y., and Yoo, C. D., 2001, “Simulation of Dynamic Behavior in a GMAW System,” Welding J., **80**, pp. 239s-245s.

[5] Wang, F., 2003, “Simulation of Metal Transfer and Weld Pool Development in Gas Metal Arc Welding of Thin Sheet Metals,” Ph.D. Thesis, University of Michigan, Ann Arbor, MI.

[6] Harlow, F. H., and Welch, J. E., 1965, “Numerical Calculation of Time-dependent Viscous Incompressible Flow of Fluid with Free Surface,” Phys. Fluids, **8**, pp. 2182-2189.

[7] Hirt, C. W., and Nichols, B. D., 1981, “Volume of Fluid (VOF) Method for the Dynamics of Free Boundaries,” J. Computational Physics, **39**, pp. 201-225.

[8] Ashgriz, N., and Poo, J. Y., 1991, “FLAIR: Flux Line-Segment Model for Advection and Interface Reconstruction”, J. Computational Physics, **93**, pp. 449-468.

[9] Brackbill, J. U., Kothe, D.B., and Zemach, C., 1992, “A Continuum Method for Modeling Surface Tension”, J. Computational Physics, **100**, pp. 335-354.

[10] Unverdi, S. O., and Tryggvason, G., 1992, “A Front-Tracking Method for Viscous, Incompressible, Mutli-fluid Flows,” J. Computation Physics, **100**, pp 25-37.

[11] Kou, S., and Sun, D. K., 1988, “Fluid Flow and Weld Penetration in Stationary Arc Welds,” Metallurgical Trans. A, **16A**, pp. 203-213.

[12] Choo, R. T. C., and Szekely, J., 1991, “The Effect of Gas Shear Stress on Marangoni Flows in Arc Welding”, Welding Journal, **70**, pp. 223s-232s.

[13] Jackson, J. D., 1962, *Classical Electrodynamics*, Wiley, New York, Chap. 10, pp. 309-311.

[14] Kim, I. S., and Basu, A., 1998, “A Mathematical Model of Heat Transfer and Fluid Flow in Gas Metal Arc Welding Process,” J. Materials Processing Technology, **77**, pp. 17-24.

[15] Peskin, C. S., 1977, “Numerical Analysis of Blood Flow in the Heart”, J. Computational Physics, **25**, pp. 220-252.

[16] Wang, Y., and Tsai, H. L., 2001, “Impingement of Filler Droplets and Weld Pool Dynamics during Gas Metal Arc Welding Process”, Int. J.Heat and Mass Transfer, **44**, pp. 2067-2080.

[17] NIST Chemistry WebBook, http://webbook.nist.gov/chemistry/

[18] Sahoo, P., DeBroy, T., and Manallan, M. J., 1988, “Surface Tension of Binary Metal-surface Active Solute Systems under Conditions Relevant to Welding Metallurgy”, Metallurgical Trans. B, **19B**, pp. 483-491.